The Astrophysical Journal, 700:1690–1701, 2009 August 1 doi:10.1088/0004-637X/700/2/1690

THE BLACK HOLE MASS, STELLAR MASS-TO-LIGHT RATIO, AND DARK HALO IN M87

Karl Gebhardt[1] and Jens Thomas[2,3]
[1] Department of Astronomy, University of Texas at Austin, 1 University Station C1400, Austin, TX 78712, USA; gebhardt@astro.as.utexas.edu
[2] Universitätssternwarte München, Scheinerstraße 1, D-81679 München, Germany
[3] Max-Planck-Institut fuer Extraterrestrische Physik, Giessenbachstrasse, D-85748 Garching, Germany; jthomas@mpe.mpg.de
Received 2008 August 19; accepted 2009 May 19; published 2009 July 16

ABSTRACT

We model the dynamical structure of M87 (NGC4486) using high spatial resolution long-slit observations of stellar light in the central regions, two-dimensional stellar light kinematics out to half of the effective radius, and globular cluster velocities out to eight effective radii. We simultaneously fit for four parameters: black hole mass, dark halo core radius, dark halo circular velocity, and stellar mass-to-light (M/L) ratio. We find a black hole mass of $6.4\,(\pm0.5) \times 10^9\ M_\odot$ (the uncertainty is 68% confidence marginalized over the other parameters). The stellar $M/L_V = 6.3 \pm 0.8$. The best-fit dark halo core radius is 14 ± 2 kpc, assuming a cored logarithmic potential. The best-fit dark halo circular velocity is 715 ± 15 km s^{-1}. Our black hole mass is over a factor of 2 larger than previous stellar dynamical measures, and our derived stellar M/L ratio is two times lower than previous dynamical measures. When we do not include a dark halo, we measure a black hole mass and stellar M/L ratio that is consistent with previous measures, implying that the major difference is in the model assumptions. The stellar M/L ratio from our models is very similar to that derived from stellar population models of M87. The reason for the difference in the black hole mass is because we allow the M/L ratio to change with radius. The dark halo is degenerate with the stellar M/L ratio, which is subsequently degenerate with the black hole mass. We argue that dynamical models of galaxies that do not include the contribution from a dark halo may produce a biased result for the black hole mass. This bias is especially large for a galaxy with a shallow light profile such as M87, and may not be as severe in galaxies with steeper light profiles unless they have a large stellar population change with radius.

Key words: galaxies: elliptical and lenticular, cD – galaxies: individual (M87, NGC4486) – galaxies: kinematics and dynamics

Online-only material: color figures

1. INTRODUCTION

M87 has been the poster child for black hole studies due to its central jet, large central velocity dispersion, and having the largest measured black hole mass. Sargent et al. (1978) and Young et al. (1978) estimate a black hole mass of $5 \times 10^9\ M_\odot$ using the surface brightness and velocity dispersion profiles. Subsequently, a large number of studies based on the stellar dynamics provide estimates from 1 to $3 \times 10^9\ M_\odot$ (see review of Kormendy & Richstone 1995). The latest estimate from Harms et al. (1994) use *Hubble Space Telescope* (*HST*) to provide a gas kinematic map and black hole estimate based on gas dynamics. Macchetto et al. (1997) analyze additional *HST* gas kinematics to derive a black hole mass of $3.2\,(\pm0.9) \times 10^9\ M_\odot$, which is considered the standard estimate for M87.

As one of the nearest galaxies and one of the largest galaxies, it is clear why M87 has had a long and important history of having its black hole mass measured. In fact, M87 is often used as the anchor for the upper end of the black hole mass distribution. There are significant consequences for understanding the value of the maximum black hole mass. It strongly affects the parameterization of the black hole mass correlations (e.g., Gültekin et al. 2009), the space density of the most massive black holes (e.g., Lauer et al. 2007), the comparison with mass derived from quasars which tend to be closer to 10^{10} rather than $10^9\ M_\odot$ (e.g., Shields et al. 2003), among many others.

A significant issue for stellar dynamical models of the black hole in M87 is that the dark halo contribution has never been included in the modeling. The latest models of the gravitational potential come from Wu & Tremaine (2006), McLaughlin (1999), Kronawitter et al. (2000), Romanowsky & Kochanek (2001), and Churazov et al. (2008). Wu & Tremaine use the globular cluster kinematics to measure the enclosed mass assuming a two-integral distribution function. McLaughlin et al. use an isotropic model for M87 based on the globular cluster kinematics and do not include a black hole. Both Kronawitter et al. and Romanowsky & Kochanek (2001) assume a spherical distribution. Churazov et al. use the gravitational potential as derived from X-ray gas and compare it to that derived from stellar dynamics. These studies find moderate agreement for the gravitational potential at large radii from the two techniques. Our goal in this paper is to understand possible degeneracies between measuring the central black hole and the dark halo simultaneously. We use orbit-based models which do not limit the form of the allowed velocity anisotropies assuming axisymmetry. We focus on M87 since the quality of the observational data for M87 has dramatically increased, and it is worthwhile to analyze it again with the most up-to-date data and dynamical models.

Our main result is that we find a black hole mass that is over two times larger when including a dark halo compared to models that do not contain a dark halo. This result is both generic in that it could be a potential concern for many of the black hole studies to date, and specific in that it applies the most up-to-date modeling to M87. Humphrey et al. (2008) model NGC 4649, a galaxy similar in mass to M87, using X-ray gas emission and find a black hole that is two times larger than the previous stellar dynamical measure of Gebhardt et al. (2003). Thus, there is a concern that black hole masses at the upper end of the distribution may be biased.

We assume a distance to M87 of 17.9 Mpc.

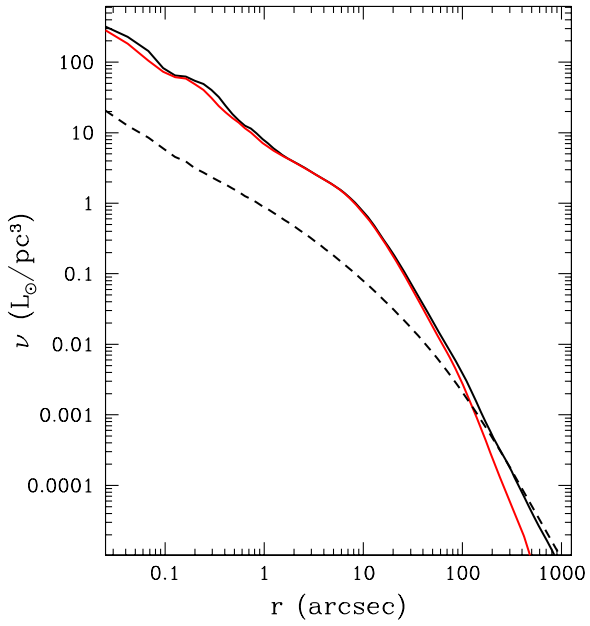

Figure 1. Volume density radial profile for stars. The black and red solid lines represent the luminosity density along the major and minor axes, respectively. These come from deprojection of the surface brightness profile presented in Kormendy et al. (2009). The dashed line is the deprojection of the surface number density for globular clusters as measured by McLaughlin (1999). The globular cluster profile is normalized, arbitrarily, to match the stellar profile in order to compare the shapes. The actual volume density of the clusters is much lower and their contribution to the stellar mass is irrelevant. Furthermore, the cluster profile within 20″ is extrapolated since there is little information to measure a surface brightness profile. Both profiles are used in the dynamical models for each of the components.

(A color version of this figure is available in the online journal.)

2. DATA

In the central regions of M87, we rely on the stellar light for both photometry and kinematics. For the outer region, the stellar kinematics only extend to about 40″. Therefore, at large radii we rely on radial velocities of individual globular clusters for the kinematics, also including the number density profile for the clusters. Unfortunately, the stellar data end around 40″ and the high signal-to-noise (S/N) globular cluster data start around 150″. Thus, there is a radial region where we presently have no kinematic data.

2.1. Stellar Density

The stellar surface density profile comes from Kormendy et al. (2009), which is a combination of *HST* data from Lauer et al. (1992) and various ground-based observations. It extends from 0.″02 to 2400″ (5 orders of magnitude). The surface brightness profile in the *V*-band, ellipticity, and position angle versus radius are shown in Kormendy et al. (2009). The ellipticity is near zero for most of the radial range, but then increases at both small and large radii. The increase at large radii has been known for some time (e.g., Weil et al. 1997), and is associated with the large rotation seen there (Kissler-Patig & Gebhardt 1998). The increase at small radii has been noted by Lauer et al. (1992) and appears to be real (as opposed to noise). In fact, the axisymmetric deprojection of the surface brightness to the luminosity density requires the increase at small radii. We deprojected the surface brightness using Magorrian (1999). This deprojection allows for a radial variation of the observed ellipticity. Figure 1 plots the luminosity density along the major and minor axes versus radius. The dynamical models use this nonparametric model of the luminosity density. From this figure one can see the increase in the ellipticity in the central region and in the outer region (the minor axis is lower than the major axis). From about 2–70″ M87 is nearly round in projection. The full radial range used in the dynamical models spans 10^7 in the luminosity density.

2.2. Stellar Kinematics

There have been many stellar kinematic studies of M87 and we rely on the two best studies for our models. These are the kinematics from SAURON (Emsellem et al. 2004) and from van der Marel (1994).

The SAURON Team provides two-dimensional kinematic coverage of M87 out to about 40″. The kinematics are parameterized with the first four coefficients of a Gauss–Hermite polynomial expansion, with uncertainties. The two-dimensional coverage of SAURON provides the best possible coverage for determining the stellar orbital structure and mass-to-light (M/L) profile. Our dynamical models fit the line-of-sight velocity distribution (LOSVD) directly as opposed to fitting to moments or Gauss–Hermite coefficients. Thus, we have to convert the SAURON velocity moments into LOSVDs; we do this by creating Monte Carlo simulations based on the uncertainties of the Gauss–Hermite coefficients. This procedure assumes that the moments are uncorrelated (further discussed in Section 4). The spatial resolution of the dynamical models is coarser than the SAURON data in the outer regions and similar in the inner regions (compare Section 3.2). Where necessary, we rebin the SAURON data by averaging, weighted by the uncertainties, over all SAURON LOSVDs in one model bin. We do not average the Gauss–Hermite coefficients. Ideally, we would not apply any spatial binning and use each ground-based element independently (even though the kinematic data was already binned originally), but this fine binning would take a significant amount of computing resources as to make the study unfeasible. We discuss the binning further in Section 3.2.

The kinematic data with the best spatial resolution come from van der Marel (1994). They have 0.″6 FWHM seeing with a 1″ slit. The data extend to 10″. van der Marel provides the first four Gauss–Hermite moments and we transform to LOSVDS as we did with the SAURON data.

Another important data set comes from Sembach & Tonry (1996), who obtain kinematics in M87 out to a radius of 130″. We do not use their kinematics mainly since they only provide velocity and velocity dispersion, without higher order moments. Since the SAURON data are such higher S/N and provide the first four moments of the LOSVD and since our modeling code fits LOSVDs (and not moments), in order to include the Sembach and Tonry data we would have to mock up the higher order moments, which would lead to additional uncertainty. Furthermore, there appears to be an offset in the velocity dispersion from Sembach and Tonry compared to other kinematic studies as discussed in Romanowsky & Kochanek (2001). Future data sets at these radii in M87 using the full LOSVD will be very important for additional analysis.

There are many other kinematic data sets, but the S/N and areal coverage of the SAURON data is so superior to all other studies that it will make little difference, if any, to the dynamical models. Given there are often systematic differences between various data sets, it is better to use just one data set. We include the van der Marel data since these add significantly to the recovery of the black hole mass. The two data sets are consistent

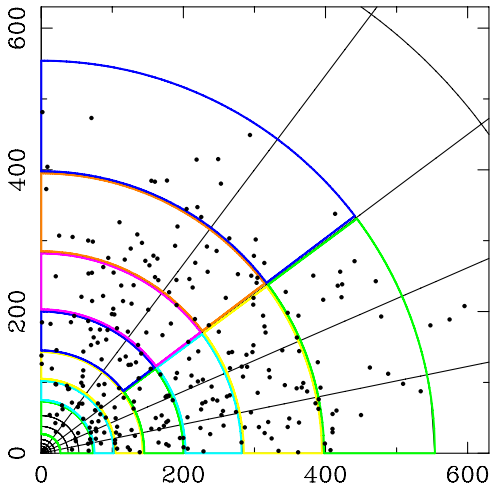

Figure 2. Grid lines represent the spatial binning used for the dynamical models. The points are the locations of the 278 globular cluster radial velocities. The black and red points represent clusters on opposite sides of the minor axis, and the red point has had its velocity flipped relative to the systemic. The colored spatial bins are the binning used for those particular cluster. Clusters outside those highlighted bins are not used in the models. There are 275 cluster velocities used for the analysis.

(A color version of this figure is available in the online journal.)

with and show no biases between each other at the radii where they overlap.

2.3. Globular Cluster Data

The surface density profile for the globular clusters comes from McLaughlin (1999), who compiles the profile based on various data sets. We deproject this profile using a nonparametric spherical inversion as described in Gebhardt et al. (1996). In Figure 1, we include a deprojected, normalized number density profile of the globular clusters; we use an arbitrary scaling for the cluster profile in order to compare the profile shapes of the clusters and stars. The total mass of the clusters is irrelevant compared to the stars. The dynamical models only use the slope of the luminosity density in order to constrain the enclosed mass. At large radii the globular cluster profile is shallower than the stellar profile, thus it is important to use the cluster profile in the dynamical models. Within 20″ there is very little information on the globular cluster profile and we must use an extrapolation there. The dashed line in Figure 1 shows what we used for the models. We have also tried two other extrapolations: one assumes a flat profile inside of 10″ and the other has a slope inside of 20″ that is equal to the stellar density. These two profiles give nearly identical results as the adopted profile.

Globular cluster velocities are reported in Cohen (2000), Cohen & Ryzhov (1997), and Hanes et al. (2001). These are compiled in Cote et al. (2001). We use the same cut as defined in Cote et al. to remove foreground and background contamination, based on velocity, color, and magnitude. These cuts result in 278 velocities.

We include the individual velocities in the dynamical models by measuring the LOSVD in different spatial regions. We divide the 278 velocities into 11 spatial bins. These spatial bins are shown in Figure 2 where we plot the model grids. Due to the nature of the spatial binning for the dynamical models, some bins will have too few clusters to be useful. At radii between 40″ and 140″ the density of clusters is low enough that we include larger bins in angle and radius than for the outer bins. Of the 278 velocities, we then use 275.

Due to the uncertain number density profile for the globular clusters in the central regions, we have run models including and excluding clusters inside of 170″. There are 68 cluster velocities in this range. Inside of 20″, there are so few clusters known (since the galaxy light begins to dominate over the cluster light), that we already have to extrapolate the number density profile. Inside of 100″, the number density is better known, but since the light profile for M87 is so shallow, deprojection errors can lead to a large effect. There are no significant changes to the best-fit values between including or excluding the central cluster velocities, but the uncertainties improve when we use more data. The largest difference, which we discuss later, is that the dark halo scale radius is much better measured.

From the approximately 25 velocities per spatial bin, we measure an LOSVD and uncertainties. The LOSVDs use an adaptive kernel density estimate adapted from Silverman (1986), and explained in detail in Gebhardt et al. (1996). The 68% confidence bands for the LOSVD come from bootstrap resamplings of the data. Another option would be to calculate moments from the individual velocities and compare the models to the moments. Since the dynamical models fit LOSVDs directly, we choose to use the measured LOSVDs. The moments derived from the measured LOSVDs compare very well with the moments derived from the individual velocities.

Since we are using an axisymmetric model, the velocities are folded along the major axis and flipped about the minor axis (the velocity relative to the systemic velocity switches sign when flipped to the opposite side of the minor axis), such that all data are placed in one quadrant. This folding preserves any rotation or angular differences at a given radius. Rotation for the globular clusters is significant at large radii (Kissler-Patig & Gebhardt 1998; Cohen 2000; Cote et al. 2001) and needs to be included for a proper dynamical model.

3. DYNAMICAL MODELS

The orbit-based models used here are described in Gebhardt et al. (2000, 2003), Siopis et al. (2009), and Thomas et al. (2004, 2005), and are based on the idea presented in Schwarzschild (1979). Similar orbit-based models are presented, for example, in Rix et al. (1997), van der Marel et al. (1998), Cretton et al. (1999), and Valluri et al. (2004). The modeling procedure consists of five steps which are further detailed below: (1) the surface brightness distribution is deprojected into a three-dimensional luminosity profile; (2) a trial gravitational potential is calculated including—in our case here—the contribution from the stars, a dark matter halo, and a black hole; (3) a large set of orbits is run in the trial potential; (4) an orbit superposition model of the galaxy in the trial potential is constructed that matches the kinematical data as good as possible subject to the constraints given by the three-dimensional light profile and the trial potential; (5) steps (1)–(4) are repeated for a large variety of trial mass profiles. A χ^2 analysis then determines the best-fit model and its uncertainties.

These models have undergone extensive tests for both recovery of the dark halo and the black hole mass. Thomas et al. (2005) describe the ability to recover the dark halo properties. Gebhardt (2004) and Siopis et al. (2009) describe the accuracy on the recovery of the black hole mass and the stellar M/L ratio. The orbit-based models show no significant bias in the recovery of the parameters for axisymmetric systems.

3.1. Model Assumptions About the Mass Distribution in M87

We calculate two different sets of dynamical models for M87 based on different assumptions about its mass structure.

In a first set of models we do not consider a dark matter halo explicitly. In fact, we assume that the M/L ratio of the galaxy is spatially constant (except at the origin):

$$\rho = \Upsilon\, \nu + M_{\rm BH}\, \delta(r), \tag{1}$$

with $M_{\rm BH}$ being the mass of the central supermassive black hole and ν being the three-dimensional light profile. If it would be true that there is no dark matter around M87 and if the M/L ratio of the stars in M87 would be constant throughout the galaxy, then Υ would be our trial value for the stellar M/L ratio. However, in fact we do expect dark matter around M87 and Υ from Equation (1) is supposed to be generally larger than the true stellar M/L ratio, because it will also account for the potential dark mass.

In our second set of models we assume that the mass distribution ρ of M87 can be written as the sum of (1) the stellar mass density, (2) a dark matter halo, and (3) a central black hole:

$$\rho = \Upsilon\, \nu + \rho_{\rm DM} + M_{\rm BH}\, \delta(r). \tag{2}$$

The dark halo is included as described in Thomas et al. (2005). We use both a logarithmic halo with a density profile given as

$$\rho_{\rm DM}(r) \propto {\rm v}_c^2 \frac{3r_c^2 + r^2}{\left(r_c^2 + r^2\right)^2}, \tag{3}$$

and a Navarro–Frenk–White (NFW) potential as given by

$$\rho_{\rm DM}(r, r_s) \propto \frac{1}{(r/r_s)(1 + r/r_s)^2} \tag{4}$$

(Navarro et al. 1996). The logarithmic halo features a flat central density core of size r_c and an asymptotically constant circular velocity v_c. The NFW profile diverges like r^{-1} toward the center and drops off with $r \propto r^{-3}$ in the outer parts, steeper than the logarithmic halo. Concentration c, scale-radius r_s, and the virial radius r_v of NFW halos are related via $c = r_v/r_s$.

3.2. Modeling the Stellar Kinematical Data

For the dynamical models of the stellar kinematics we use a spatial binning with $N_r = 28$ radial and $N_\vartheta = 5$ angular bins, respectively (compare Gebhardt et al. 2000 for more details on the spatial grids). Figure 2 plots the radial and azimuthal plot of the spatial binning. The model bins are generally larger than the SAURON bins and, in that case, we average the SAURON LOSVDs as described in Section 2.2. After the spatial binning we have $N_{\mathcal{L}}^{\rm stars} = 6+46$ LOSVDs (van der Marel & SAURON). Each of these stellar LOSVDs $\mathcal{L}^{\rm stars}$ is sampled by $N_{\rm vel} = 19$ velocity bins.

For each trial potential (compare Equations (1) and (2)) we determine the weighted orbit superposition that has the lowest

$$\chi^2_{\rm stars} = \sum_{i=1}^{N_{\mathcal{L}}^{\rm stars}} \sum_{j=1}^{N_{\rm vel}} \left(\frac{\mathcal{L}_{ij}^{\rm stars} - \mathcal{L}_{ij}^{\rm mod}[\nu]}{\Delta \mathcal{L}_{ij}^{\rm stars}} \right)^2. \tag{5}$$

Here, $\mathcal{L}_{ij}^{\rm mod}[\nu]$ is the model LOSVD in the spatial bin j. During the χ^2 minimization, the orbit model is forced to reproduce the three-dimensional luminosity profile ν with machine precision. This ensures that the final model is self-consistent, i.e., that the generated dynamical model supports those orbits out of which it is constructed.

When two orbits differ in their spatial shape only on a sub-bin scale, then they are equivalent with respect to the density constraints, but their projected kinematics may be different. Then, a slight change in the potential parameters can be compensated for by shifting light from one orbit to the other, without affecting the density constraints. That our model bins are larger than the SAURON data therefore likely increases the uncertainties of the derived mass parameters with respect to the optimum that could have been achieved given the observational data. However, the overall mass budget of an axisymmetric dynamical model is determined (1) by the density constraints and (2) by the total amount of kinetic energy along the line of sight (Thomas et al. 2007a). Since Figure 3 shows that there is no significant variation of the velocity dispersion over any of our model bins, the total kinetic energy along the line of sight is conserved after the rebinning. Furthermore, Siopis et al. (2009) and Thomas et al. (2005) perform tests of recovery of black hole mass and dark halo profile for analytic models. Using the same modeling code as used here and a similar binning scheme, they find accurate recovery of the input parameters. Thus, we do not expect that the chosen spatial binning used here introduces a significant bias to the mass recovery.

3.3. Modeling the Globular Cluster Kinematics

The globular cluster system can have a different orbital structure than the system of the stars, such that we need to model the globular cluster velocities separately from the stars. However, the models for the GC system are very similar to the models of the stellar kinematics. In particular, we use the same mass models (compare Equation (2), we do not attempt to model the GC kinematics without a dark matter halo). The only difference is that the weighted orbit superposition in each trial potential is determined by minimizing

$$\chi^2_{\rm GC} = \sum_{i=1}^{N_{\mathcal{L}}^{\rm GC}} \sum_{j=1}^{N_{\rm vel}} \left(\frac{\mathcal{L}_{ij}^{\rm GC} - \mathcal{L}_{ij}^{\rm mod}[n_{\rm GC}]}{\Delta \mathcal{L}_{ij}^{\rm GC}} \right)^2, \tag{6}$$

where $\mathcal{L}^{\rm GC}$ are the $N_{\mathcal{L}}^{\rm GC} = 11$ globular cluster LOSVDs from Section 2.3 and $n_{\rm GC}$ is the deprojected number–density profile of the GCs. When minimizing the above $\chi^2_{\rm GC}$, we force the models to reproduce $n_{\rm GC}$ with machine precision.

In contrast to the stars, we treat the GCs of M87 as a system of massless test particles. Therefore, in principle we do not need to reproduce $n_{\rm GC}$ with machine precision, as any mismatch in $n_{\rm GC}$ would not have any effect on the potential. However, we have tried three profiles for $n_{\rm GC}$ with different central slopes and find nearly identical results. As discussed earlier, the more important aspect is whether we include the globular cluster velocities inside of 170″ where the density of observed velocities begins to decrease. The analysis presented here use all of the central globular cluster velocities. However, models that exclude the central velocities show no change in the best-fit values, but increase the uncertainties. The largest change is for the dark matter scale radius since when the central velocities are included we find an increase in the uncertainty by about 50%.

3.4. Constraining the Mass Density in M87

In total we fit for four sets of models: (1) we fit only for the black hole mass and stellar Υ including the SAURON and van

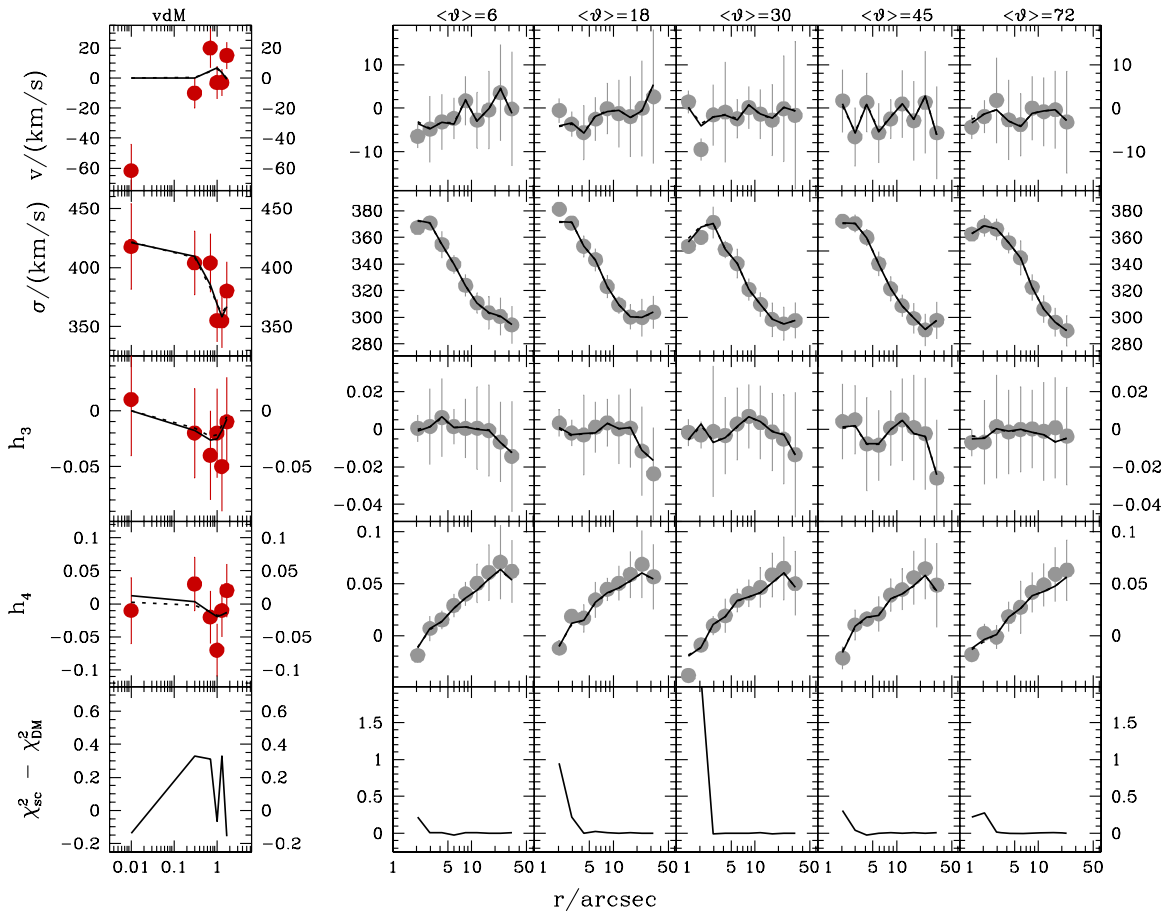

Figure 3. Velocity v, velocity dispersion σ, and Gauss–Hermite coefficients h_3, h_4 as a function of radius. Points with errors bars: observational data from van der Marel (red; left column) and SAURON (gray; columns on the right-hand side; each column corresponds to one angular bin of the models; the mean latitude is quoted on top); solid lines: best-fit model with dark matter halo; dotted lines: best-fit model without dark matter. Bottom row: χ^2 difference between the best-fit with dark halo ($\chi^2_{\rm DM}$) and without ($\chi^2_{\rm sc}$). Positive values in the bottom row indicate that the model with dark matter fits better.

(A color version of this figure is available in the online journal.)

der Marel data only (no globular cluster data and assuming no dark halo), which mimics what has been done for most black hole mass studies, (2) we fit black hole mass, stellar Υ, and two dark halo parameters using the SAURON data and van der Marel data only, (3) we fit black hole mass, stellar Υ, and two dark halo parameters using the globular cluster data only, and (4) we fit black hole mass, stellar Υ, and two dark halo parameters using the SAURON data, van der Marel data, and the globular cluster kinematics. For the last set of models we combine the constraints from the stellar and the GC kinematics by minimizing the sum $\chi^2_{\rm stars} + \chi^2_{\rm GC}$. Note that because the stars and the GCs sample different spatial scales of M87, the best-fit models (2), (3), and (4) are not the same.

For the models (1) without dark matter halo we have to determine two free parameters: Υ and $M_{\rm BH}$ (compare Equation (1)). However, when including a dark matter halo, the amount of parameter coverage (with four parameters and two sets of potentials) is large. We start with a uniform, sparse grid in this four-dimensional parameter space. Then we iteratively sample on a finer grid, focusing on the region(s) around the smallest χ^2. Specifically, during iteration n we determine all models closer to the best-fit than $\Delta\chi^2 \leqslant 1$. We then extend the sampling around these models by filling the 80 adjacent grid points around each of them. In this way, iteration n closes the surface in parameter space around all models with $\Delta\chi^2 \leqslant 1$ of iteration $n-1$. After the last iteration our fine grid covers the entire $\Delta\chi^2 \leqslant 1$ region. We also finely sampled a region that is not at the minimum to assure that the sampling is adequate in all areas of χ^2; this denser sampling can be seen in the figures described below (Figures 4 and 5), and we find that our sampling procedure adequately represents the minimum χ^2 contours over the four parameters.

We have run over 25,000 orbit libraries with about 25,000 orbits per library, and each model takes approximately 1.5 hr of cpu. We use the Texas Advanced Computing Center (TACC) at the University of Texas at Austin, where they have a cluster of over 5000 nodes.

4. RESULTS

We first discuss models for M87 excluding the contribution from a dark halo. All black holes measured to date exclude the contribution from a dark halo (e.g., Gebhardt et al. 2003), so these models provide a good comparison. The best-fitted M/L_V is 10.2 ± 0.4, and the best-fitted black hole mass is $2.3(\pm 0.6) \times 10^9 M_\odot$. Both of these values are consistent with previous dynamical determinations (as compiled in Kormendy & Richstone 1995; Cappellari et al. 2006). The model is compared to the data in Figure 3 (dotted lines). It provides a good fit to the data.

Including the dark halo significantly increases the parameter space that has to be explored. Given that we run over 10,000 models with four parameters it is difficult to visualize the χ^2

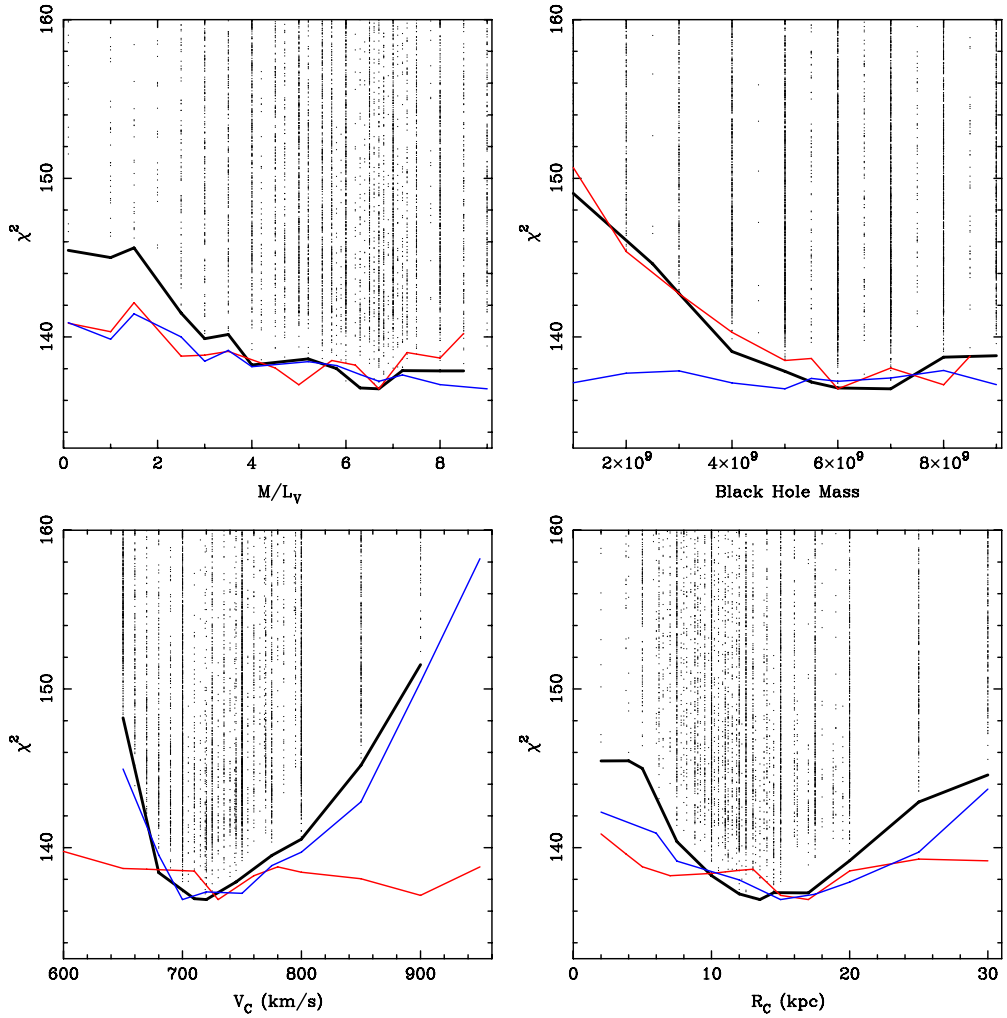

Figure 4. χ^2 vs. the four parameters. In each panel, we plot all models vs. one of the parameters. A trace along the bottom ridge thus represents the marginalized χ^2 distribution, which we use to determine the best fit and uncertainties. The small points represent all models for the logarithmic potential. The solid lines are the marginalized χ^2 values for three models. The red line is the χ^2 determined from stars only; the blue line comes from clusters only; the black line is from the combination. We note that the black line is not a sum of the red and blue lines. The value of the χ^2 (the vertical axes) are for the combined value, and that for stars and clusters have been shifted in order to see detail in the χ^2 contours. In the plot, for the stars, we add 26.3 to the χ^2, and for the clusters we add 114.2. The differential χ^2 values are preserved.

(A color version of this figure is available in the online journal.)

distribution with a single plot. Figure 4 plots the χ^2 versus each of the four parameters, including all values of the other three parameters. For each panel the contour that follows the envelope of minimum values is the marginalized χ^2, and is what we use for the estimation of the parameters and their uncertainties.

4.1. χ^2 Analysis

The combined $\chi^2 = \chi^2_{\rm stars} + \chi^2_{\rm GC}$, which we use to constrain the gravitational potential. Figure 4 plots the χ^2 values for the stars only, globular clusters only, and for the combined sample. The red line in the figure is for the stars ($\chi^2_{\rm stars}$); the blue line is for the clusters ($\chi^2_{\rm GC}$); the black line is for the combination. The values on the y-axis are the sum of χ^2 for the stars and clusters. In order to plot the individual χ^2 from the stars and clusters, we must vertically shift their values; since we only use an additive shift, the relative χ^2 is preserved. A value of 26.3 is added to the χ^2 for the stars, and 114.2 for that of the clusters. We note that the black line is not the sum of the blue and red lines, since the model with the smallest χ^2 in the sum will not be the same model for the one that gives the minimum when using either stars or clusters only. For the stars, with 52 LOSVDs that we use in the models and since each are generated from four Gauss–Hermite parameters, the total number of parameters is 208. For the clusters, there are 11 LOSVDs, with about four independent values, adding another 44 parameters. Thus, the reduced χ^2 is about 0.65. This number is similar to what we find for orbit-based models (Gebhardt et al. 2003), which may be due to a correlation among the Gauss–Hermite coefficients (e.g., Houghton et al. 2006).

It is clear from Figure 4 that the stars are primarily responsible for determining the black hole mass and that the clusters are responsible for determining the circular velocity of the dark matter. The stellar M/L comes primarily from the stars, but it has a significant degeneracy with the dark halo (see below). The scale radius of the dark halo is actually determined from both stars and clusters.

Figure 4 provides the values of the best-fit parameters and uncertainties. For the uncertainties we use $\Delta\chi^2 = 1$ for each parameter when marginalizing over the other three parameters.

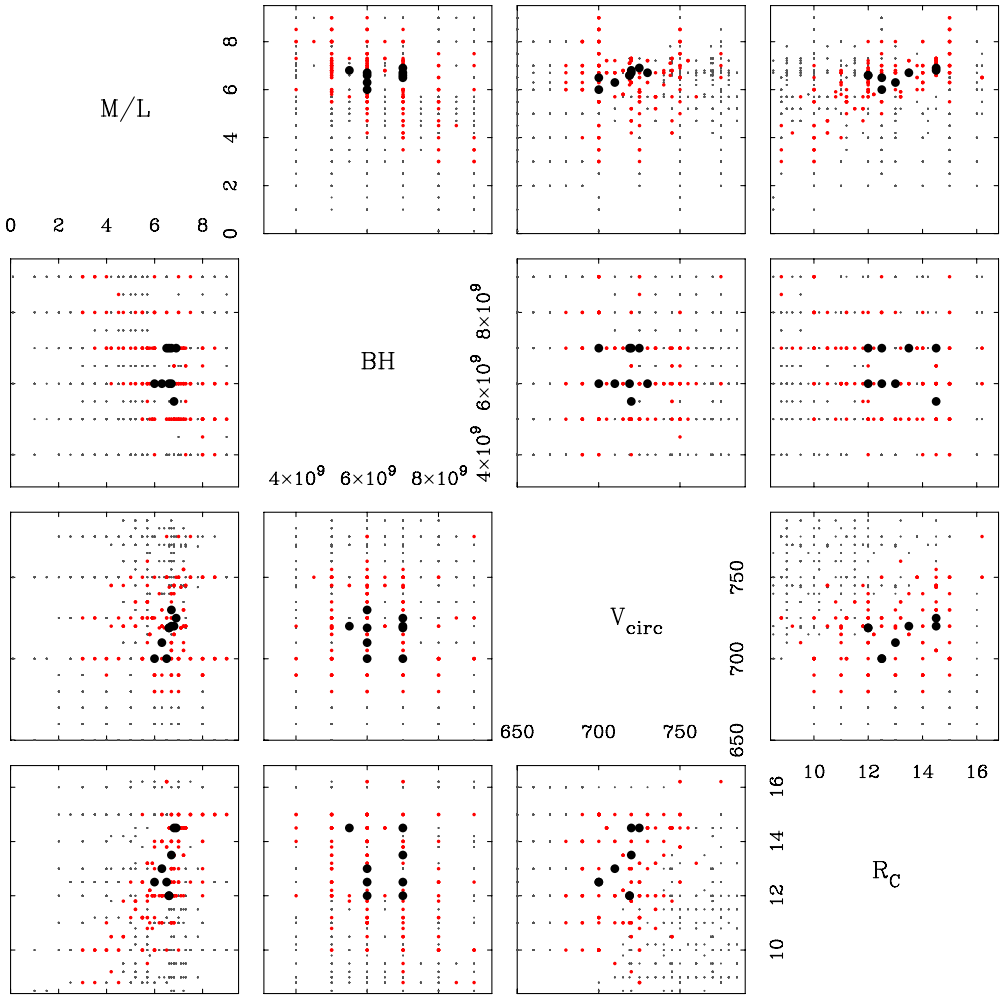

Figure 5. Plots of the four parameters against each other, designed to show possible degeneracies. The parameters are: M/L in the V band, black hole mass in $M_{\odot}$, circular velocity of a logarithmic halo in km s^{-1}, and core radius of the logarithmic halo in kpc. The plotting range is chosen to highlight the region around the best fit for each parameter. The small gray points represent the locations of all the models; there are many additional models beyond the plotting range that all provide significantly worse fits. The large black points are the locations of those models that are within the 68% confidence limit after marginalizing over the other parameters (i.e., $\Delta\chi^2 = 1.0$). The red points are those that are within the 95% confidence band. The only panel that shows an obvious correlation is the one with core radius against M/L (the upper right plot), which is due to the trade between the mass of dark matter and stars. The correlation between stellar M/L and black hole mass is weak within the 68% bands shown here, but becomes significant for the 95% confidence band.

(A color version of this figure is available in the online journal.)

We determine the range of those models within the 68% limit and use the middle of the range as the best-fit and half of the range as the uncertainty. For black hole mass we find $6.4\,(\pm0.5) \times 10^9\ M_{\odot}$; for stellar M/L_V we get $6.3\,(\pm0.8)$; for logarithmic halo circular velocity we find $715\,(\pm15)$ km s^{-1}; for dark halo scale radius we get $14.0\,(\pm2.0)$ kpc. Our best-fit model with dark matter halo is compared to the data in Figure 3 (solid lines). In the outer parts, models with and without dark matter fit almost equally well to the SAURON data, reflecting that the information about the halo comes mostly from the GC kinematics. However, the model with dark matter halo fits better in the inner regions (both to the van der Marel and the inner SAURON data). This indicates that there is a significant change in the dynamical M/L ratio from $M/L_V \approx 10$ at $r = 40''$ to $M/L_V \approx 6$ at $r \approx 3''$. Toward the very center, the two models again become very similar, which is (1) due to the large uncertainties in the van der Marel data and (2) due to the degeneracy between stellar M/L and black hole mass.

Our results could be biased by the choice of the dark halo parameterization. In particular, since we use a profile with a flat central density core, our models are entirely dominated by luminous mass in the inner regions. Then, in the center the luminous mass is degenerate with the black hole mass and, in the outer parts, the luminous mass is degenerate with the halo (see also the discussion below), but there is no direct communication between halo and black hole. The situation would be different when using a cuspy halo profile, which could lead to models with a significant amount of dark mass near the center, such that halo and black hole mass could be directly degenerate. To check for this, we have also run models for NFW. The grid used for the NFW models is rather coarse (we use about 1/10 of the sampling used for the logarithmic potential) and a finer grid would be more informative, but the general shape of χ^2 versus the four parameters is similar. It turns out that realistic NFW fits (that fit the GC kinematics) are not centrally concentrated enough to dominate the mass in the inner regions and, thus, the mass profiles we get with NFW fits are very similar to those obtained with logarithmic halos. (Note also, that the central logarithmic slope of the deprojected light profile is close to -1 and, thus, comparably steep as the cusp of the NFW core.) That

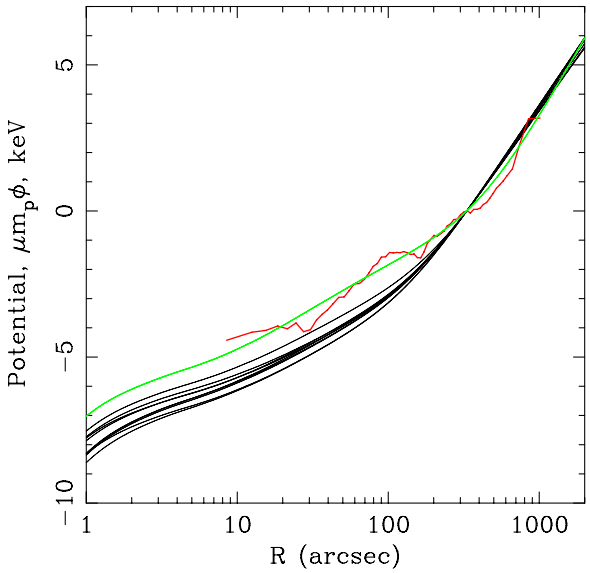

Figure 6. Gravitational potential vs. radius for M87. The solid black lines are the dynamical models from this paper that are within the 68% confidence band of the best fit. The red noisy line is the gravitational potential as derived from the X-ray gas emission from Churazov et al. (2008). The green solid line is the parameterization from our models that well matches the X-ray profile (the parameters of the matched model are $6 \times 10^9\ M_\odot$, 8.0, 800 km s^{-1}, 35 kpc for black hole mass, M/L_V, circular velocity, and core radius, respectively. The difference in χ^2 between our representation of the X-ray potential and that of the best fit is 18. The units of the potential are as given in Churazov et al. and all models are scaled to $R = 330''$.

(A color version of this figure is available in the online journal.)

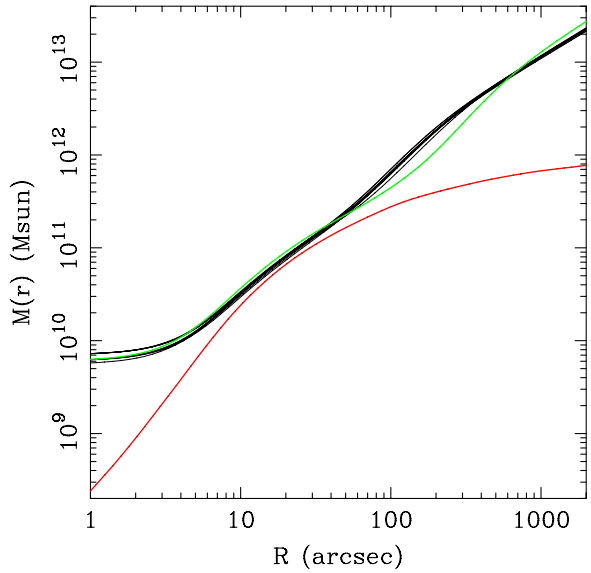

Figure 7. Mass profile for M87. The black lines represent the models that are within the 68% confidence band of the best fit (as in Figure 6). The green line is the mass profile derived from our representation of the X-ray gravitational potential (i.e., the green line in Figure 6). The red line is the average contribution from the stars, where we use the light profile 6.3 times that in Figure 1 (the best-fitted M/L). The mass profiles for the dynamical model show a smooth transition from 30 to 1000″, whereas the X-ray profile shows a kink.

(A color version of this figure is available in the online journal.)

fits with NFW and logarithmic halos yield similar results has also been found in other early-type galaxies (Thomas et al. 2005, 2007). Since the results are similar, we do not discuss results from NFW models.

Figure 5 plots the relationships between the four parameters for the models. The parameter space is much larger than shown in this figure since we only focus on the region around the best fit. In each panel, we include all models that are in that parameter range, irregardless of their χ^2 values. The color and symbol size, however, indicate those models that are within the 68% ($\Delta\chi^2 = 1$ after marginalizing over the other three parameters) and the 95% ($\Delta\chi^2 = 4$) confidence bands of the best-fitted model. The idea is to explore any correlations/degeneracies among the parameters. There is not an obvious correlation between M/L and black hole mass in the plotted region around the minimum χ^2. However, increasing the confidence band to 95% shows a correlation. This degeneracy is expected. Since the dynamical models only fit for the enclosed mass, as the contribution from the stars is increased in the central region, the contribution from the black hole has to decrease. An obvious degeneracy within the 68% band is that between M/L and scale radius of the halo. As the scale radius is decreased, for a given circular velocity, the contribution of the dark matter in the central regions is increased, thereby decreasing the contribution from the stars. These degeneracies are the essential reason why the dark halo properties affect the inferred black hole mass in M87. Beyond the plotting region, there are no points within the 68% confidence region, which allows us to set reasonable uncertainties on the parameters.

4.2. Gravitational Potential

Figure 6 plots the gravitational potential. The black lines are the potentials of the models that are within the 68% limit ($\Delta\chi^2 = 1$ for the marginalized parameters). We also plot the gravitational potential as inferred from the X-ray profile as presented in Churazov et al. (2008). These have all been scaled to be zero at 330″ as in Churazov et al. The red line is the model from Churazov et al. and it is clearly dissimilar from the best-fit potential derived from the stellar and cluster dynamics. The green line is one of the models we used which is close to the gravitational potential from the X-rays; we use that model to represent the X-ray profile in subsequent analysis. Between the green line and the best-fitted model, $\Delta\chi^2 = 18$, which implies the potential derived from the X-ray is significantly poorer fit to the kinematics. We find a potential that is deeper than the X-ray derived potential. Churazov et al. (2008) explore a shock model for the X-rays in an attempt to explain the wiggles seen in the X-ray potential, but this model would not explain the large offset. Additional galaxies with potentials derived from both stars and X-rays will be important to study. This difference in the potential may be specific to M87.

4.3. Enclosed Mass and M/L Ratio

Figure 7 plots the enclosed mass. The black lines represent the models that are within the 68% confidence limit. The enclosed mass flattens in the center due to the black hole and rises linearly due to the dark halo. The red line is the stellar contribution assuming $M/L = 5.0$. The green line is the enclosed mass from our model which best matches the gravitational potential derived from the X-rays. In the potential derived from the X-rays (green line in Figure 6), there is a transition around 300″ from the steep profile beyond that to a shallow profile inside of that radius. This transition manifests itself as a wiggle in the enclosed mass profile around 200–300″. The enclosed mass derived from the stellar kinematics instead show a very smooth gradient from a few arcseconds out to 1000″. If enclosed mass profiles are relatively smooth, as the one derived here, it will be fairly easy to constrain that profile using a nonparametric approach.

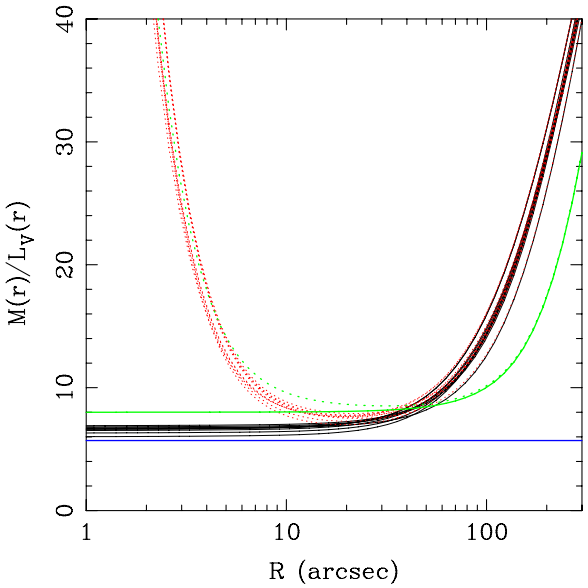

Figure 8. Integrated M/L vs. radius. The red dotted lines represent the models that are within the 68% confidence band of the best-fitted potentials (black lines in Figure 6). The solid black lines are the same models excluding the contribution from the black hole. The green solid and dotted lines are our best representation of the X-ray potential without and with a black hole. The horizontal blue line is the M/L derived from stellar population models. From the red dotted lines, there is no radial region in M87 that has a constant M/L, since one always has to consider the contribution from either black hole or dark halo.

(A color version of this figure is available in the online journal.)

This approach would be much cleaner to implement since the kinematics only measure enclosed mass. By trying to constrain the stellar contribution to the mass and the dark halo contribution leads to degeneracies as seen in the above figures. However, this alternative approach would require some simplification of the enclosed mass profile in order to use a reasonable amount of cpu time (e.g., the four parameters explored above required about 20,000 hr).

Figure 8 plots the integrated M/L ratio. We include all models within the 68% confidence limit of the best-fitted model. M/L profiles for these models are shown as the red dotted lines in the figure. The increase at small radius is from the black hole and the increase at large radius is from the dark halo. There is no region in M87 where the M/L is constant. The solid black lines in Figure 8 are the M/L profiles including just the stars and dark halo, and are intended to show the range of stellar M/L values. Figure 8 also plots the M/L profile from our representation of the X-ray potential, both without (solid green) and with (dashed green) a black hole. The blue horizontal line is the best-fitted value of the stellar M/L from stellar population models (Cappellari et al. 2006). The stellar population models use Kroupa initial mass function (IMF) with lower mass cutoff of 0.01. The stellar population models may have a large range of M/L values depending on the lower mass cutoff. The adopted value of 0.01 is quite low and may bias the M/L's high if the lower cutoff is more massive.

5. DISCUSSION

There are a variety of results from this work, some determined more robustly than others. Very robust results are (1) the black hole mass in M87 from stellar dynamical measures is over two times higher when including a dark halo, (2) the dynamical stellar M/L is two times lower when including a dark halo, and (3) uncertainties on parameters significantly increase when including a dark halo. A model-dependent result from this work, although still very significant, is that (4) the gravitational potential derived from X-rays for M87 is inconsistent with that derived from kinematics. Below we discuss each of these points and their implications.

5.1. Black Hole Mass

One of the more robust results from this work is the increase in the black hole due to inclusion of the dark matter halo. The reason is quite simple: dynamical models only measure enclosed mass and if, in the central regions, one lowers the stellar contribution with a smaller M/L, then that mass must be compensated by a corresponding increase in the black hole mass. For M87, since the light profile is so shallow, the dynamically derived M/L value will contain information from stars that spend most of their time at large radii where the dark halo dominates. Thus, excluding a halo will result in pushing the M/L higher to match the observed velocity dispersions. One could partially compensate for this by excluding kinematics at large radii in a dynamical analysis. This may work somewhat for some galaxies, but as seen in Figure 8, there is no region in M87 where there is a constant M/L, causing a need to model simultaneously the black hole and the dark halo.

A concern from this work could be that the dark halo parameters are poorly constrained by the globular cluster kinematics, leading to a biased result due to the above degeneracy. We have therefore run a grid of models assuming the potential derived from the X-rays and fitting for black hole mass and stellar M/L. We find nearly identical results when fitting for the dark halo as well. The dark halo that we derived is only moderately more massive than the one from X-rays, but using either gives the same answer for the black hole mass. This is reassuring as it leads to a clean result for the black hole mass. Thus, we are confident that in M87 the black hole mass is $6.4\,(\pm0.5) \times 10^9\ M_\odot$ derived from stellar kinematics.

There are significant implications for having a black hole mass this large. There has long been an issue as to why black hole masses derived from quasars can exceed $10^{10}\ M_\odot$, whereas the masses derived from local galaxies never approach that. M87 and NGC4649 (Gebhardt et al. 2003; Humphrey et al. 2008) have the largest measured black holes around $3 \times 10^9\ M_\odot$. The space density of quasars with massive black holes imply that we should have many black holes approaching 10^{10} out to about 100 Mpc (Shields et al. 2003). Many studies have pointed out this problem (e.g., Richstone et al. 1998; Shields et al. 2003; Lauer et al. 2007; Bernardi et al. 2007; Salviander et al. 2008). With a black hole mass of $6.4 \times 10^9\ M_\odot$, the agreement between the space density of the most massive black holes is in closer agreement with that derived from quasars. Because this change is due to an issue in the modeling (and not sample selection) and because only one object can have such a large effect, it is not worthwhile at this point to do a detailed comparison. A much better approach would be to re-examine the other massive galaxies and study additional ones.

Another implication of biased and larger black hole masses is the effect it will have on correlations of the black hole mass with global galaxy properties. The correlation of black hole with velocity dispersion (Gebhardt et al. 2000; Ferrarese & Merritt 2000) has led to a large amount of theoretical research as to the cause of the correlation and the value of the slope (e.g., Hopkins et al. 2007). If the measured black holes at the upper are biased

low, this will obviously have a significant lever arm on the value of the slope and scatter. The black hole masses were already high and possibly hint at a curvature in the relation (Wyithe 2006, and see the recent analysis of Gültekin et al. 2009). Correlations with other parameters would also need re-evaluating. Again, it is not prudent to re-analyze the current sample in regards to the correlations until the bias is understood well with both re-examinations and larger samples.

There is a difference of the black hole mass measured with our analysis compared to the previous *HST* gas kinematic measure. Macchetto et al. (1997) use gas kinematics measured with *HST* to derive a black hole mass of $3.2\,(\pm0.9) \times 10^9\,M_\odot$. They use a distance of 15 Mpc. Transforming to our assumed distance of 17.9 Mpc gives a mass of $3.8\,(\pm0.9) \times 10^9$. The radii of the gas emission is in a region that is dominated by the black hole, so there is little difference if the stellar M/L changes, as we measure in this paper. For the black hole mass, 6.4 ± 0.5 compared to 3.8 ± 0.9 is only a 2σ difference and while that may not be statistically significant, it is important to consider possible causes for the difference. There have been very few studies of galaxies with black hole masses measured from both stars and gas. Of those that do have both measures, the results can vary greatly: IC1459 has the gas measure eight times larger than that of the stars (Cappellari et al. 2002) and CenA has the stellar measure seven times larger than that of the gas (Silge et al. 2005; Neumayer et al. 2007), although Cappellari et al. (2009) show that they are consistent for CenA. The maser galaxy, NGC4258, has a consistent mass estimate (Siopis et al. 2009), although using the masing gas is not the same as using the gas further out. Ho et al. (2002) discuss ways to optimize the use of gas kinematics for measuring the black hole mass by focusing on those galaxies with well-organized dust lanes. For M87, the gas disk is not very well defined (see Macchetto et al. 1997) and the uncertainties with the inclination can be large, but it would be difficult to have inclination explain all of the difference. More significant concerns with using the gas kinematics is that the intrinsic density distribution is poorly constrained and the gas emission lines usually show large velocity broadenings that are not generally considered. For M87, Macchetto et al. include an estimate of the density distribution but there are clearly large uncertainties since many volume density distributions can project to give similar projected densities. Macchetto et al. model the line centroids of the gas emission to determine the gravitational potential. For their assumed intrinsic gas distribution (which has a hole in the center), they also match the large velocity dispersions seen in the emission lines; however, the unknown intrinsic distribution can strongly affect the gas centroids and dispersions. The problem is that it is not clear whether one should include the velocity broadening (thereby assuming a hot component to the gas orbits) or exclude them (assuming some type of turbulent motion), as discussed in Verdoes Kleijn et al. (2006). For M87, this effect could account for some of the difference.

The resolution of the difference between the gas kinematics and the stellar kinematics will best come from stellar kinematic data taken with better spatial resolution. Whatever the value of the black hole mass, however, the dynamical models show a strong effect between including and excluding a dark halo when the influence of the black hole is not well resolved.

5.2. Stellar M/L

The stellar M/L_V that we derive without a dark halo is 10 (9.7 correcting for extinction) and with a dark halo is 6.3 (5.3 correcting for extinction). This is a very significant difference, but it is obvious as to why that happens since the dynamical models simply are trading enclosed mass in stars with enclosed mass in dark matter. Adopting the gravitational potential as derived from the X-rays requires a stellar M/L of 8, but this model provides a significantly worse fit than our best fit. We compare to M/L as derived from stellar population models. Cappellari et al. (2006) use Kroupa IMF to derive $M/L_I = 3.33$ and find a dynamically derived $M/L_I = 6.1$, using $A_B = 0.1$ and distance of 15.6 Mpc. Transforming to V band and 17.9 distance implies $M/L_V = 5.2$ (stellar population) and $M/L_V = 9.6$ (dynamical). Our dynamically derived M/L is in good agreement with that derived from the stellar population models. Also, when we exclude the dark halo, we find a very similar M/L as the dynamically derived M/L from Cappellari et al. who do not include a dark halo. Thus, the M/L derived from stellar population models supports our conclusion that the dark halo is important for deriving the proper M/L and, subsequently, the black hole mass.

The physical understanding of the fundamental plane is affected by the dark matter fraction as a function of galaxy mass, which implies being able to measure the stellar M/L. Until more galaxies are examined at this level of detail (as in Thomas et al. 2007b), we do not attempt to address implications for the fundamental plane.

5.3. Parameter Uncertainties

As we increase the number of parameters in the dynamical models, the uncertainties on those parameters will also increase. In fact, there are some parameters which we have not explored for M87. Two important ones include inclination and triaxiality. For inclination, if M87 is spherical, then it should not have a large effect. However, if M87 is very flattened and seen face-on, inclination will be important; although since galaxies with the mass of M87 are all seen as nearly round, the likelihood is that they are spherical. In addition, M87 is flattened at large radii. Triaxiality is a bigger concern, since these large galaxies tend to be triaxial in numerical simulations (although no conclusive evidence yet either way from observations). Triaxial models (van den Bosch et al. 2008) have only recently been developed, and it will be important to study M87 as a triaxial system. The uncertainties play a key role in understanding the physical nature of the black hole correlations. Including a dark halo already increased the uncertainties on the black hole and particularly on the stellar M/L. Thus, until additional analysis on the degeneracies is explored and a larger sample is included, it would be prudent to include a modest systematic bias uncertainty for the black hole mass estimates when studying the correlations and their intrinsic scatter.

5.4. Dark Halo and X-Ray Properties

It is generally assumed that the X-ray emitting gas can be used as a robust tracer of the gravitational potential, and there have been studies that show rough agreement between the two (as shown in Churazov et al. 2008). However, all of the dynamical studies rely on fairly restrictive assumptions about the stellar distribution function: Wu & Tremaine (2006) assume a two-integral distribution function, McLaughlin (1999) assume spherical isotropic distribution function, and both Kronawitter et al. (2000) and Romanowsky & Kochanek (2001) assume a spherical distribution. Given that the stellar density profile at large radii is very flattened and that the globular clusters show

significant rotation, it is important to explore more general models as the ones presented here. We find rough agreement with the enclosed mass at some locations in M87, but the shape of the potential profile is quite different. The gravitational potential in Figure 6, in fact, shows fairly significant differences between the two derived potentials. This figure, however, is not as fair a comparison since the dynamical models directly measure the enclosed mass and it is more instructive to focus on that aspect. Since the enclosed mass is a derivative of the potential, one needs to focus on the change in shape of Figure 6; for $R < 40''$, the derivative of the potential is very similar, which subsequently leads to good agreement with the enclosed mass. At $R > 600''$, there is also good agreement in the enclosed mass (and derivative of the potential). But it is the radii from $40 < R < 600$ where there is the strongest disagreement, since the potential derived from X-rays shows a strong kink there while that derived from stellar kinematics shows a smooth transition. This region is where there is no stellar data with modest coverage by globular cluster kinematics; however, given that we are using parametric models for the dark matter profile, it is a robust result that the X-ray potential is a significantly worse fit to the data than the best-fit logarithmic potential. It is clear though that additional data at these radii are very much needed. We note that the kinematics of Sembach & Tonry (1996) are more consistent with our best-fitted profile than with the X-ray profile; however, the uncertainties are large and better data are needed to make the comparison conclusive.

The dark halo parameters are, for a logarithmic potential, a circular velocity of 715 ± 15 km s^{-1} and a core radius of 14 ± 2 kpc (similar to Kronawitter et al. 2000). This halo is similar to those measured in Thomas et al. (2007b) and Gerhard et al. (2001) in terms of the circular velocity but M87 has a smaller core radius for galaxies of somewhat smaller mass. We also ran a smaller grid of potentials that follow an NFW profile. The best fitted parameters were around a concentration of 15 and a scale radius of 50 kpc. We do not provide uncertainties since we did not explore a very dense grid. Using either NFW or logarithmic, the potential derived from X-rays was statistically excluded.

M87 may not be the best case where X-ray gas emission provides an adequate representation of the potential. The X-ray potential shows significant deviations from a smooth curve, and Churazov et al. (2008) use these deviations to derive a jet model, with cooling and heating regions. This model, however, does not explain the difference at $40 < R < 600''$. It would be important to study other galaxies that do not show the strong deviations seen in M87, but it is possible that the X-ray gas in M87 may not be an adequate tracer of the potential.

5.5. Next Steps

There are a variety of ways to move forward. On the data side, there is a strong need for observations at small radii using observations assisted with adaptive optics on a large telescope. The faint central surface brightness of M87 made it not possible to observe with the spectrographs on *HST*, but it is an ideal target for ground-based telescopes. It should be straightforward to detect a black hole with as high a mass as presented in this paper. At larger radii, there is a critical need to obtain stellar kinematics in the region from $40 < R < 300''$. This is feasible using current ground-based instruments (e.g., VIRUS-P on the 2.7 m telescope at McDonald Observatory; Hill et al. 2008). The large radial data will strongly limit dark halo models, and allow us to not rely as heavily on the kinematics from the small number of globular clusters. Both of these observational avenues, at small and large radii, are in progress.

On the modeling side, it would be worthwhile to include more general models, such as triaxiality, and an exploration of inclination. For this paper, we use a parametric form for the dark halo and there is little theoretical justification for such an approach. A cleaner approach would be to use a nonparametric estimate for the enclosed mass, such as a mass profile defined in radial bins. This method would directly include any change of mass-to-light ratio of the stars. The enclosed mass is directly measured from the kinematics, and then interpretation of how to split between stars and dark halo could come subsequently. Given that the enclosed mass profile is relatively smooth (Figure 7), it should be an easy matter to constrain it. However, with just four parameters, it was already a large computer effort, which could obviously increase dramatically as the number of fitted mass bins increase.

There is a strong need to explore additional galaxies. It could be that since M87 has no region where there is a constant M/L (see Figure 8), that the degeneracies between black hole and dark halo, mediated by the stellar M/L become very large. Galaxies with smaller black holes and/or smaller relative fraction of dark halo should be studied with this type of analysis.

Whether or not the dark halo parameters presented here correctly reflect reality (we obviously agree that they do), we performed a simple test of measuring the black hole with the same modeling code including and excluding a dark halo. In a differential sense, the importance of including the dark halo is one of the strongest and cleanest results. All black holes measured, to date, including those of the authors (Gebhardt et al. 2003) exclude a dark halo (see discussion in Nowak et al. 2008). While we expect that M87 shows the largest effect due to its shallow light profile, we are at the point now where the details of the black hole correlations are important and understanding all biases are therefore essential.

K.G. thanks the Max-Planck-Institut fuer Extraterrestrische Physik and Carnegie Institute of Washington for their excellent support and hospitality. K.G. is very grateful to John Kormendy who has been pushing for a few years to understand any possible degeneracy between black hole mass and dark halo. We are grateful for conversations with Ralf Bender, Douglas Richstone, Scott Tremaine, and Tod Lauer. We would not have attempted this analysis without the publically available two-dimensional data set from SAURON; it is a tremendous service to the community that the SAURON team choose to make the data public and in an easy to use format. The project would not have been possible without the excellent facilities at the Texas Advanced Computing Center at The University of Texas at Austin, which has allowed access to over 5000 node computers where we ran all of the models. K.G. acknowledges NSF-CAREER grant AST03-49095.

REFERENCES

Bernardi, M., Sheth, R., Tundo, E., & Hyde, J. 2007, ApJ, 660, 267
Cappellari, M., et al. 2002, ApJ, 578, 787
Cappellari, M., et al. 2006, MNRAS, 366, 1126
Cappellari, M., et al. 2009, MNRAS, 394, 660
Churazov, E., Forman, W., Vikhlinin, A., Tremaine, S., Gerhard, O., & Jones, C. 2008, MNRAS, 388, 1062
Cohen, J. 2000, AJ, 119, 162
Cohen, J., & Ryzhov, A. 1997, ApJ, 486, 230
Cote, P., et al. 2001, ApJ, 559, 828

Cretton, N., de Zeeuw, P.T., van der Marel, R., & Rix, H.-W. 1999, ApJS, 124, 383
Emsellem, E., et al. 2004, MNRAS, 352, 721
Ferrarese, L., & Merritt, D. 2000, ApJ, 539, L9
Gebhardt, K. 2004, in Carnegie Observatories Astrophysics Series 1, Coevolution of Black Holes and Galaxies, ed. L. C. Ho (Cambridge: Cambridge Univ. Press), 249
Gebhardt, K., et al. 1996, AJ, 112, 105
Gebhardt, K., et al. 2000, ApJ, 539, L13
Gebhardt, K., et al. 2003, ApJ, 583, 92
Gerhard, O., Kronawitter, A., Saglia, R. P., & Bender, R. 2001, AJ, 121, 1936
Gültekin, K., et al. 2009, ApJ, 698, 198
Hanes, D., et al. 2001, ApJ, 559, 812
Harms, R., et al. 1994, ApJ, 435, L35
Hill, G. J., et al. 2008, Proc. SPIE, 7014, 257
Ho, L. C., Sarzi, M., Rix, H.-W., Shields, J., Rudnick, G., Filippenko, A., & Barth, A. 2002, PASP, 114, 137
Hopkins, P., et al. 2007, ApJ, 669, 45
Houghton, R., Magorrian, J., Sarzi, M., Thatte, N., Davies, R., & Krajnovic, D. 2006, MNRAS, 367, 2
Humphrey, P., Buote, D., Brighenti, F., Gebhardt, K., & Mathews, W. 2008, ApJ, 683, 161
Kissler-Patig, M., & Gebhardt, K. 1998, AJ, 116, 2237
Kormendy, J., Fisher, D., Cornell, M., & Bender, R. 2009, ApJS, 182, 216
Kormendy, J., & Richstone, D. 1995, ARA&A, 33, 581
Kronawitter, A., Saglia, R., Gerhard, O., & Bender, R. 2000, A&AS, 144, 53
Lauer, T., et al. 1992, AJ, 103, 703
Lauer, T., et al. 2007, ApJ, 662, 808
Macchetto, F., Marconi, A., Axon, D., Capetti, A., Sparks, W., & Crane, P. 1997, ApJ, 489, 579
Magorrian, J. 1999, MNRAS, 302, 530
McLaughlin, D. 1999, AJ, 117, 2398
Navarro, J. F., Frenk, C. S., & White, S. D. M. 1996, ApJ, 462, 563
Neumayer, N., Cappellari, M., Reunanen, J., Rix, H.-W., van der Werf, P., deZeeuw, P. T., & Davies, R. 2007, ApJ, 671, 1329
Nowak, N. 2008, MNRAS, 301, 1629
Richstone, D., et al. 1998, Nature, 395, 14
Rix, H.-W., et al. 1997, ApJ, 488, 702
Romanowsky, A., & Kochanek, C. 2001, ApJ, 553, 722
Salviander, S., Shields, G., Gebhardt, K., Bernardi, M., & Hyde, J. 2008, AJ, 687, 828
Sargent, W. L. W., Young, P., Lynds, C. R., Boksenberg, A., Shortridge, K., & Hartwick, F. D. A. 1978, ApJ, 221, 731
Schwarzschild, M. 1979, ApJ, 232, 236
Sembach, K., & Tonry, J. 1996, AJ, 112, 797
Shields, G., et al. 2003, ApJ, 583, 124
Silge, J., Gebhardt, K., Bergmann, D., & Richstone, D. 2005, AJ, 130, 406
Siopis, C., et al. 2009, ApJ, 693, 946
Silverman, B. W. 1986, Density Estimation for Statistics and Data Analysis (New York: Chapman & Hall)
Thomas, J., Jesseit, R., Naab, T., Saglia, R., Burkert, A., & Bender, R. 2007a, MNRAS, 381, 1672
Thomas, J., Saglia, R., Bender, R., Thomas, D., Gebhardt, K., Magorrian, J., Corsini, E., & Wegner, G. 2005, MNRAS, 360, 1355
Thomas, J., Saglia, R., Bender, R., Thomas, D., Gebhardt, K., Magorrian, J., Corsini, E., & Wegner, G. 2007b, MNRAS, 382, 657
Thomas, J., Saglia, R., Bender, R., Thomas, D., Gebhardt, K., Magorrian, J., & Richstone, D. 2004, MNRAS, 353, 391
Valluri, M., Merritt, D., & Emsellem, E. 2004, ApJ, 602, 66
van den Bosch, R., van de Ven, G., Verolme, E., Cappellari, M., & de Zeeuw, P. T. 2008, MNRAS, 385, 647
van der Marel, R. 1994, MNRAS, 270, 271
van der Marel, R., Cretton, N., de Zeeuw, P. T., & Rix, H.-W. 1998, ApJ, 493, 613
Verdoes Kleijn, G., van der Marel, R. P., & Noel-Storr, J. 2006, AJ, 131, 1961
Weil, M., Bland-Hawthorn, J., & Malin, D. 1997, ApJ, 490, 664
Wu, X., & Tremaine, S. 2006, ApJ, 643, 210
Wyithe, J. S. 2006, MNRAS, 365, 1082
Young, P. J., Westphal, J. A., Kristian, J., Wilson, C. P., & Landauer, F. P. 1978, ApJ, 221, 721